



Production of neutron-rich actinide isotopes in isobaric collisions via multinucleon transfer reactions

Peng-Hui Chen¹ · Chang Geng¹ · Zu-Xing Yang² · Xiang-Hua Zeng^{1,3} · Zhao-Qing Feng⁴

Received: 25 May 2023 / Revised: 19 June 2023 / Accepted: 10 July 2023 / Published online: 31 October 2023

© The Author(s), under exclusive licence to China Science Publishing & Media Ltd. (Science Press), Shanghai Institute of Applied Physics, the Chinese Academy of Sciences, Chinese Nuclear Society 2023

Abstract

We systematically calculated the multinucleon transfer reactions of ^{208}Os , ^{208}Pt , ^{208}Hg , ^{208}Pb , ^{208}Po , ^{208}Rn , ^{208}Ra , and $^{132,136}\text{Xe}$ when bombarded on ^{232}Th and ^{248}Cm at Coulomb barrier energies within the dinuclear system model. These results are in good agreement with the available experimental data. The influence of Coulomb and shell effects on actinide production in these reactions has been rigorously studied. We calculated and analyzed the potential energy surface (PES) and total kinetic energy (TKE) mass distributions for the reactions involving ^{208}Hg , ^{208}Pb , and ^{208}Po with ^{248}Cm and ^{232}Th . The PES and TKE spectra shed light on the fragment formation mechanisms in multinucleon transfer reactions, with clear indications of isospin and shell effects. The production cross sections for multinucleon transfer products show a strong dependence on isobar projectiles with a mass number $A = 208$. Isobar projectiles with high N/Z ratios are advantageous for generating neutron-rich target-like fragments. Conversely, products induced by isobar projectiles with larger charge numbers tend to shift toward proton-rich regions. The intertwining of the Coulomb potential and shell effect is evident in the production cross sections of actinide isotopes. Drawing from reactions induced by radioactive projectiles, we anticipate the discovery of several new actinide isotopes near the nuclear drip lines, extending our reach into the superheavy nuclei domain.

Keywords Dinuclear system model · Isobaric collisions · Multinucleon transfer reactions · Neutron-rich actinides

1 Introduction

To date, the synthesis of 11 isotopes— ^{149}Lu [1], ^{207}Th [2], $^{251,264}\text{Lr}$ [3, 4], ^{166}Pm , ^{168}Sm , ^{170}Eu , ^{172}Gd [5], ^{204}Ac [6], ^{39}Na [7], and ^{286}Mc [8]—in the last year, has brought the total count to 3327 known nuclei in the nuclide chart. This comprises 288 natural nuclides (254 stable isotopes with lifespans longer than the Earth's age and 34 unstable nuclides) and 3039 species of nuclei synthesized in global laboratories. These syntheses utilize techniques such as fusion-evaporation (FE), multinucleon transfer (MNT), deep-inelastic reactions (DIR), projectile fragmentation (PF), spallation, fission (SF), neutron capture (NC), and thermonuclear tests (TT) [9]. However, various theoretical models predict the existence of an additional 8000 to 10,000 unknown bound isotopes in the nuclei chart [10–12]. This suggests that at least over 5000 nuclides remain to be discovered by nuclear experimentalists, particularly in the realms of nuclear drip lines and the stability islands of superheavy nuclei.

In recent years, laboratories across the globe have made significant advancements in nuclear synthesis. From an

This work was supported by National Natural Science Foundation of China (Nos. 12105241, 12175072), Natural Science Foundation of Jiangsu Province (No. BK20210788), Jiangsu Provincial Double-Innovation Doctoral Program (No. JSSCBS20211013), University Science Research Project of Jiangsu Province (No. 21KJB140026), Lv Yang Jin Feng (No. YZLYJFJH2021YXBS130), and Key Laboratory of High-Precision Nuclear Spectroscopy, Institute of Modern Physics, Chinese Academy of Sciences (No. IMPKFKT2021001).

✉ Peng-Hui Chen
chenpenghui@yzu.edu.cn

¹ School of Physical Science and Technology, Yangzhou University, Yangzhou 225009, China

² RIKEN Nishina Center, Wako, Saitama 351-0198, Japan

³ College of Electrical, Power and Energy Engineering, Yangzhou University, Yangzhou 225009, China

⁴ School of Physics and Optoelectronics, South China University of Technology, Guangzhou 510641, China

experimental standpoint, several new nuclear species have been produced: ^{207}Th , ^{235}Cm , ^{214}U , ^{222}Np , ^{211}Pa , ^{280}Ds [2, 13–15], and others via fusion-evaporation (FE) reactions; ^{110}Zr , ^{121}Tc , ^{129}Pd , and more through projectile fragmentation (PF) [16]; and $^{223,229}\text{Am}$, ^{233}Bk [17], among others, using multinucleon transfer (MNT) reactions. This study has garnered significant attention from leading research facilities, including the Lanzhou Heavy Ion Research Facility (HIRFL) in China, Joint Institute for Nuclear Research (JINR) in Russia, Helmholtz Centre for Heavy Ion Research (GSI) in Germany, Grand Accélérateur National d'Ions Lourds (GANIL) in France, and Argonne National Laboratory (ANL) in the USA, actively working toward the synthesis of new nuclides in regions near the drip lines and within the superheavy region.

In efforts to elucidate the damped collision mechanism and predict the synthesis cross sections of target nuclides, theorists have crafted intricate yet pragmatic models to represent the multinucleon transfer reactions occurring at incident energies close to the Coulomb barrier. Notable among these are the GRAZING model [18–20], the dinuclear system (DNS) model [21–30], and a dynamical model anchored in the Langevin equations [31, 32]. There are also microscopic methods that account for the degrees of freedom inherent to nucleons. Examples include the time-dependent Hartree (TDHF) approach [33–35] and the improved quantum molecular dynamics model (ImQMD) [36, 37]. Although each model possesses its distinctive attributes, they are all capable of faithfully replicating available experimental data. The DNS model, in particular, offers a comprehensive view, considering factors, such as the shell effect, dynamic deformations, fission, quasi-fission, deep-inelastic mechanisms, and the odd-even effect. Furthermore, it stands out for its exceptional computational efficiency.

In this study, we compared the calculated cross sections of target-like fragments resulting from MNT reactions of $^{132,136}\text{Xe} + ^{248}\text{Cm}$ at incident energies proximate to the Coulomb barriers with the available experimental data, using the DNS model as a basis. To delve into the interplay between the Coulomb force and shell effect in the MNT process, we selected isobaric projectiles with a mass number $A = 208$ in proximity to the double magic nucleus ^{208}Pb . These projectiles were directed to bombard targets ^{232}Th and ^{248}Cm at energies consistent with the Coulomb barrier. Our analysis further explores the production cross sections of yet-to-be-identified actinide isotopes in isobaric collisions. The structure of this study is as follows: In Sect. 2, we provide a concise overview of the DNS model. Section 3 presents the calculation results and subsequent discussion. Finally, a summary and conclusions drawn from our study are detailed in Sect. 4.

2 Model description

Initially, Volkov introduced a concept to depict deep-inelastic heavy-ion collisions [38]. Later on, Adamian incorporated a quasi-fission component into the massive fusion process [39, 40]. Subsequent enhancements, including modifications to the relative motion energy and angular momentum of the colliding nuclei, in tandem with nucleon transfer, were developed within the DNS framework by the Lanzhou Group [41]. The production cross sections of superheavy nuclei (SHN), quasi-fission, and fusion–fission dynamics have been comprehensively examined within the dynamical DNS model. The dynamic evolution of the colliding system involves sequential processes: overcoming the Coulomb barrier to form the DNS, adjusting the relative motion energy, angular momentum, mass, charge asymmetry, among other factors, within the potential energy surface, and finally, the de-excitation of primary fragments [42]. The production cross section of the MNT fragments was determined as follows:

$$\sigma_{\text{tr}}(Z_1, N_1, E_{\text{c.m.}}) = \sum_{J=0}^{J_{\text{max}}} \sigma_{\text{cap}}(E_{\text{c.m.}}, J) \int f(B) \times P(Z_1, N_1, J_1, B) \times W_{\text{sur}}(E_1, J_1, s) dB. \quad (1)$$

$\sigma_{\text{cap}}(E_{\text{c.m.}}, J)$ denotes the cross section of the DNS formation derived by the Hill–Wheeler formula with a barrier distribution function [43]. $W_{\text{sur}}(E_1, J_1, s)$ denotes the survival probability of the fragment formation during the MNT process. Furthermore, s denotes the decay channels for fragments (Z_1, N_1) such as neutrons, protons, deuteron, alpha rays, and gamma rays. $E_{\text{c.m.}}$ denotes the incident energy at the center-of-mass frame. The highest angular momentum J_{max} was calculated for the colliding system in the grazing configuration. The angular momentum J was considered at the initial collision configuration before dissipation. E_1 and J_1 denote the excitation energy and angular momentum of the fragment with proton number Z_1 and neutron number N_1 , respectively, in DNS, respectively. Additionally, $P(Z_1, N_1, J_1, B)$ is the formation probability of fragments (Z_1, N_1) . For the barrier distribution function, we adopted an asymmetric Gaussian [44] form.

$$f(B) = \frac{1}{N} \exp \left[- \left(\frac{B - B_m}{\Delta} \right)^2 \right] \quad (2)$$

The quantities Δ and B_m were evaluated using $\Delta = (B_t + B_s)/2$ and $B_m = (B_t + B_s)/2$. Furthermore, B_t and B_s represent the height of the Coulomb barrier and minimum point of deformation under tip–tip collision, respectively. The normalization constant satisfies $\int f(B) dB = 1$.

In the DNS model, the solution for nucleon transfer and relative motion involves a set of microscopic derivations, and the master equations distinguish between protons and neutrons. The fragment distribution probability, $P(Z_1, N_1, E_1)$, represents the proton number Z_1 , neutron number N_1 , and excitation energy E_1 for DNS fragment 1, which is described by the following master equation:

$$\begin{aligned} & \frac{dP(Z_1, N_1, E_1, \beta, t)}{dt} \\ &= \sum_{Z'_1} W_{Z_1, N_1, \beta; Z'_1, N_1, \beta'}(t) [d_{Z_1, N_1} P(Z'_1, N_1, E'_1, \beta', t) \\ & \quad - d_{Z'_1, N_1} P(Z_1, N_1, E_1, \beta, t)] \\ & \quad + \sum_{N'_1} W_{Z_1, N_1, \beta; Z_1, N'_1, \beta'}(t) [d_{Z_1, N_1} P(Z_1, N'_1, E'_1, \beta', t) \\ & \quad - d_{Z_1, N'_1} P(Z_1, N_1, E_1, \beta, t)] \\ & \quad - [\Lambda_{A_1, E_1, t}^{\text{qf}}(\Theta) + \Lambda_{A_1, E_1, t}^{\text{fis}}(\Theta)] P(Z_1, N_1, E_1, t) \end{aligned} \tag{3}$$

Specifically, $W_{Z_1, N_1, \beta; Z'_1, N_1, \beta'}(W_{Z_1, N_1, \beta; Z_1, N'_1, \beta'})$ is the mean transition probability from channel (Z_1, N_1, E_1, β) to $(Z'_1, N_1, E'_1, \beta')$, [or (Z_1, N_1, E_1, β) to $(Z_1, N'_1, E'_1, \beta')$], and d_{Z_1, N_1} denotes the microscopic dimension corresponding to the macroscopic state (Z_1, N_1, E_1) . The sum is considered over all possible proton and neutron numbers that fragment (Z'_1, N'_1) may take; however, only one nucleon transfer is considered in the model, with the relations $Z'_1 = Z_1 \pm 1$ and $N'_1 = N_1 \pm 1$. The quasi-fission width Λ^{qf} and fission width Λ^{fis} were calculated using Kramers formula [45, 46].

The excited DNS creates a valence space where the valence nucleons are symmetrically distributed around the Fermi surface. Only particles in states within this valence space participate actively in nucleon transfer. The local excitation energy and nucleon transfer influence the transition probability. These are microscopically determined from the interaction potential within the valence space, as detailed in [47, 48].

$$\begin{aligned} W_{Z_1, N_1, \beta; Z'_1, N_1, \beta'} &= \frac{\tau_{\text{mem}}(Z_1, N_1, \beta, E_1; Z'_1, N_1, \beta', E'_1)}{d_{Z_1, N_1} d_{Z'_1, N_1} \hbar^2} \\ & \times \sum_{ii'} |\langle Z'_1, N_1, E'_1, i' | V | Z_1, N_1, E_1, i \rangle|^2. \end{aligned} \tag{4}$$

The neutron transition coefficient has the same formula. The relaxation time is calculated using the deflection function method [49]. The memory time τ_{mem} and V interaction elements can be found in [47].

The motion of the nucleons in the interacting potential is governed by a single-particle Hamiltonian [41, 50]:

$$H(t) = H_0(t) + V(t) \tag{5}$$

with

$$H_0(t) = \sum_K \sum_{\nu_K} \epsilon_{\nu_K}(t) \alpha_{\nu_K}^+(t) \alpha_{\nu_K}(t) \tag{6}$$

$$\begin{aligned} V(t) &= \sum_{K, K'} \sum_{\alpha_K, \beta_{K'}} u_{\alpha_K, \beta_{K'}} \alpha_{\alpha_K}^+(t) \alpha_{\beta_{K'}}(t) \\ &= \sum_{K, K'} V_{K, K'}(t) \end{aligned} \tag{7}$$

Here, indices K and K' ($K, K' = 1, 2$) denote fragments 1 and 2, respectively. Furthermore, quantities ϵ_{ν_K} and $u_{\alpha_K, \beta_{K'}}$ represent the single-particle energy and interaction matrix elements, respectively. Single-particle states are defined with respect to the centers of the interacting nuclei and are assumed to be orthogonalized in the overlap region. Thus, the annihilation and creation operators depend on the time. The single-particle matrix elements are parameterized as follows:

$$u_{\alpha_K, \beta_{K'}} = U_{K, K'}(t) \left\{ \exp \left[-\frac{1}{2} \left(\frac{\epsilon_{\alpha_K}(t) - \epsilon_{\beta_{K'}}(t)}{\Delta_{K, K'}(t)} \right)^2 \right] - \delta_{\alpha_K, \beta_{K'}} \right\}. \tag{8}$$

Detailed calculations of these parameters and the mean transition probabilities are described in Ref. [41, 50].

$$\Delta \epsilon_K = \sqrt{\frac{4\epsilon_K^*}{g_K}}, \quad \epsilon_K^* = \epsilon^* \frac{A_K}{A}, \quad g_K = A_K/12, \tag{9}$$

where ϵ^* denotes the local excitation energy of the DNS. The microscopic dimensions of fragment (Z_K, N_K) were evaluated using the valence states $N_K = g_K \Delta \epsilon_K$ and valence nucleons $m_K = N_K/2$ ($K = 1, 2$) as:

$$d(m_1, m_2) = \binom{N_1}{m_1} \binom{N_2}{m_2}. \tag{10}$$

The local excitation energy E_1 was derived from the dissipation energy coupled to the potential energy surface (PES) of the relative motion of the DNS. The excitation energy in the equilibrium stage was determined by dividing the fragments by their mass. The angular momentum of the main fragment was determined by the moment of inertia. The local excitation energy was evaluated using [47, 48]

$$\epsilon^*(t) = E^{\text{diss}}(t) - (U(\{\alpha\}) - U(\{\alpha_{\text{EN}}\})). \tag{11}$$

The quantities of the entrance channel, denoted as α_{EN} , encompass proton and neutron numbers, quadrupole deformation parameters, and orientation angles. Specifically, they are represented as $Z_p, N_p, Z_T, N_T, R, \beta_p, \beta_T, \theta_p,$ and θ_T for the projectile and target nuclei by symbols P and T, respectively. The interaction time τ_{int} is obtained using the deflection function method [51]. The energy dissipated in the DNS

exhibits an exponential increase. The potential energy surface (PES) of the DNS can be evaluated as follows:

$$U_{\text{dr}}(t) = Q_{\text{gg}} + V_{\text{C}}(Z_1, N_1; \beta_1, Z_2, N_2, \beta_2, t) + V_{\text{N}}(Z_1, N_1, \beta_1; Z_2, N_2, \beta_2, t) + V_{\text{def}}(t) \quad (12)$$

with

$$V_{\text{def}}(t) = \frac{1}{2} C_1 (\beta_1 - \beta'_T(t))^2 + \frac{1}{2} C_2 (\beta_2 - \beta'_P(t))^2 \quad (13)$$

$$C_i = (\lambda - 1)(\lambda + 2) R_{\text{N}}^2 \delta - \frac{3}{2\pi} \frac{Z^2 e^2}{R_{\text{N}}(2\lambda + 1)}. \quad (14)$$

where Q_{gg} , derived from the negative binding energies of fragments (Z_i, N_i), was calculated using the liquid-drop model plus shell correction [11]. θ_i denotes the angle between the collision orientations and symmetry axes of the deformed nuclei. Furthermore, V_{C} and V_{N} were calculated using Wong's formula [52] and the double-folding potential [53], respectively. The quadrupole deformations of the ground-state nuclei were obtained from Ref. [54]. Additionally, $V_{\text{def}}(t)$ denotes the deformation energy of DNS at reaction time t . The evolutions of quadrupole deformations of the projectile- and target-like fragments occur from the initial configuration as

$$\begin{aligned} \beta'_T(t) &= \beta_T \exp(-t/\tau_\beta) + \beta_1 [1 - \exp(-t/\tau_\beta)], \\ \beta'_P(t) &= \beta_P \exp(-t/\tau_\beta) + \beta_2 [1 - \exp(-t/\tau_\beta)] \end{aligned} \quad (15)$$

where the deformation relaxation was $\tau_\beta = 4 \times 10^{-21}$ s.

The total kinetic energy (TKE-mass) of the primary fragment was evaluated using the following expression:

$$\text{TKE} = E_{\text{c.m.}} + Q_{\text{gg}} - E^{\text{diss}}, \quad (16)$$

where $Q_{\text{gg}} = M_{\text{P}} + M_{\text{T}} - M_{\text{PLF}} - M_{\text{TLF}}$ and $E_{\text{c.m.}}$ denote the incident energy in the center-of-mass frame. Masses M_{P} , M_{T} , M_{PLF} , and M_{TLF} correspond to the projectile, target, projectile-like fragment, and target-like fragment, respectively.

The survival probability $W_{\text{sur}}(E_1, J_1, s)$ is particularly important in the evaluation of the cross section, which is usually calculated using a statistical model. The physical process for understanding excited nuclei is straightforward. However, the magnitude of the survival probability is strongly dependent on the ingredients in the statistical model, such as the level-density parameter [55], separation energy [54], shell correction [54], and fission barrier [56, 57], and others. The excited fragments were cooled by evaporating γ -rays and light particles (including neutrons, protons, and α particles) in competition with fission [44]. The probability in the channel for evaporating the x th neutron, y th proton, and z -alpha particle can be expressed as follows:

$$W_{\text{sur}}(E_1^*, x, y, z, J) = P(E_1^*, x, y, z, J) \times \prod_{i=1}^x \frac{\Gamma_{\text{n}}(E_i^*, J)}{\Gamma_{\text{tot}}(E_i^*, J)} \prod_{j=1}^y \frac{\Gamma_{\text{p}}(E_j^*, J)}{\Gamma_{\text{tot}}(E_j^*, J)} \prod_{k=1}^z \frac{\Gamma_{\alpha}(E_k^*, J)}{\Gamma_{\text{tot}}(E_k^*, J)}, \quad (17)$$

where E_1^* and J denote the excitation energies evaluated from the mass tables in Ref. [11] and spin of the excited nucleus, respectively. The total width Γ_{tot} is the sum of the partial widths of the particle evaporation, γ emission, and fission. The excitation energy E_s^* before evaporating the s th particle can be evaluated as follows:

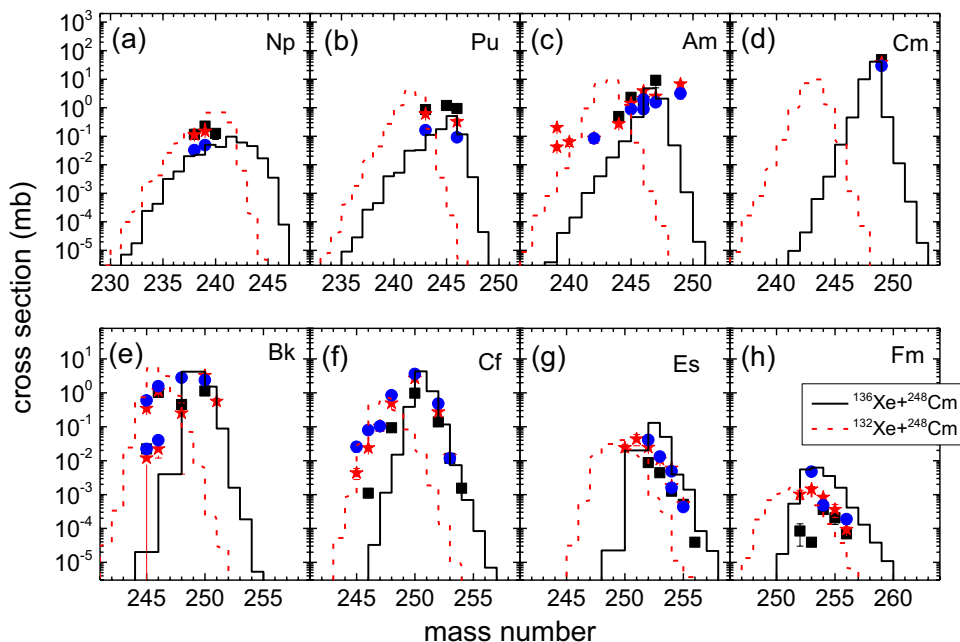
$$E_{s+1}^* = E_s^* - B_i^{\text{n}} - B_j^{\text{p}} - B_k^{\alpha} - 2T_s, \quad (18)$$

where the initial conditions are E_1^* and $s = i + j + k$. Furthermore, B_i^{n} , B_j^{p} , and B_k^{α} are the separation energies of the i th neutron, j th proton, and k th alpha, respectively. The nuclear temperature T_i is obtained by $E_i^* = aT_i^2 - T_i$, where a denotes the level-density parameter. The fission and particle decay widths were calculated using the Weisskopf evaporation theory and Bohr–Wheeler formula, respectively. The realization probability $P(E_1^*, x, y, z, J)$ was calculated using Jackson's formula [58].

3 Results and discussion

We calculated the production cross sections of actinide isotope chains with atomic number $Z = 93$ –100 in the collisions of $^{132,136}\text{Xe} + ^{248}\text{Cm}$ at incident energy $E_{\text{lab}} = 699$ –790 MeV, as shown in Fig. 1. Compared with the available experimental data for $^{129,132,136}\text{Xe} + ^{248}\text{Cm}$, which are represented by a solid red star, solid blue circle, and solid black squares with error bars, respectively, our calculation of $^{136}\text{Xe} + ^{248}\text{Cm}$, marked by solid black lines, and $^{132}\text{Xe} + ^{248}\text{Cm}$, marked by dashed red lines, could reproduce the tendency of the cross-sectional distribution of actinide isotopic chains. From experimental data [59, 60], it was determined that projectile $^{129,132,136}\text{Xe}$ isotopes-induced reactions with the target ^{248}Cm to provide actinide products that have a large overlap distribution area in the neutron-rich region. This was not clearly distinguishable as expected. From our calculation in terms of the deep-inelastic mechanism, relative proton-rich projectile ^{132}Xe -induced reactions tend to shift to the proton-rich region when compared to the experimental results. Based on the data presented in Fig. 1, target-like fragments have production cross sections of magnitude levels from 100 millibarns to 10 nanobarns. When significantly distanced from the target, the formation cross section of products below the target declines more gradually than that of trans-target products. This suggests that quasi-fission plays a more dominant role in these collisions. It is worth noting that our calculations have limitations: They rely on a model with free

Fig. 1 (Color online) Calculation and experiment results of production cross sections of actinide isotopic chains with $Z = 93-100$ in reactions of $^{129,132,136}\text{Xe} + ^{248}\text{Cm}$ at $E_{\text{lab}} = 699-790$ MeV. The available experimental data are considered from [59, 60], marked by solid black square for ^{136}Xe -induced reactions, solid red star for ^{132}Xe -induced reactions, solid blue circle for ^{129}Xe -induced reactions. Our calculations for ^{136}Xe -induced reactions were shown by solid black lines, ^{132}Xe -induced reactions shown by dashed red lines



parameters both for calculating the primary fragment cross section and for estimating the survival probability against fission.

To investigate the competition between the Coulomb repulsive potential and shell effect in MNT reactions, we calculated the reactions of isobaric projectiles with $A = 208$ bombarding targets ^{248}Cm and ^{232}Th at incident energy $E_{\text{c.m.}} = 1.1 \times V_B$. The calculation details of these collisions are presented below. The interaction potential between the colliding partners was combined with the Coulomb and nuclear potentials. In Fig. 2a, interaction potential V_{CN}

of $^{208}\text{Pt} + ^{248}\text{Cm}$, $^{208}\text{Hg} + ^{248}\text{Cm}$, $^{208}\text{Pb} + ^{248}\text{Cm}$, $^{208}\text{Po} + ^{248}\text{Cm}$, and $^{208}\text{Rn} + ^{248}\text{Cm}$ reactions was marked by solid black, dashed red, dash-dot blue, dash-dot-dot green, and short dashed olive lines, respectively. The tendencies of V_{CN} distributions for these collisions were similar. A larger Coulomb potential results in a larger interaction potential V_{CN} . Specifically, V_{CN} increases exponentially with decreasing distance R decreasing in the attraction region of the nuclear force, where it increases slowly. Nucleon transfer occurred in the touch configuration. Based on the deflection function,

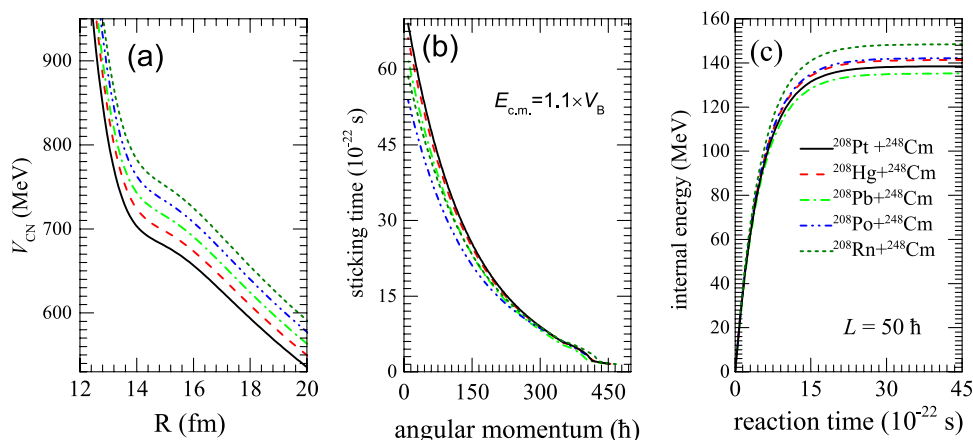


Fig. 2 (Color online) In panel a, solid black, red, blue, green, olive lines indicate the interaction potential of the tip-tip collisions as a function of surface distance in reactions induced by projectiles ^{208}Hg , ^{208}Pb , ^{208}Po , ^{208}Pt , and ^{208}Rn , respectively, with target ^{248}Cm ; Panel b shows distributions of reaction time to the angular momen-

tum of collisions for these five reaction systems at incident energy $E_{\text{c.m.}} = 1.1 \times V_B$, which decreases exponentially as angular momentum increases. In panel c, for a given angular momentum $L = 50\hbar$ across these five collision systems, the internal excitation energies are shown to increase exponentially with reaction time

the sticking times of the colliding partners are calculated for all impact parameters [49], as shown in Fig. 2b, which decreases exponentially as angular momentum increases. In these collisions, a relatively large Coulomb potential resulted in a longer sticking time with a fixed impact parameter. During the sticking time, the kinetic energy dissipates into the composite system to heat with the internal excitation energy, which increases exponentially with reaction time and reaches equilibrium at approximately 2×10^{-21} s, as shown in Fig. 2c.

After the colliding partners are captured, the dissipated kinetic energy, combined with the angular momentum in the DNS, allows them to diffuse along the potential energy surface (PES). This is followed by nucleon rearrangement between the colliding entities, determined by solving a set of master equations. The PES and driving potential were derived using Eq. (12). These are composed of the Coulomb potential, binding energy, and nuclear potential. They are calculated using the Wong formula, the liquid-drop model with shell correction, and the double-folding method, respectively, as cited in [42]. The driving potential of projectiles ^{208}Hg , ^{208}Pb , and ^{208}Po on targets ^{248}Cm and ^{232}Th during tip–tip collision at a fixed distance is plotted as a function of mass asymmetry, denoted as η . Here, $\eta = (A_T - A_P)/(A_T + A_P)$. This is illustrated in Fig. 3a, e, represented by solid black, dashed red, and dash-dot blue lines, respectively.

Open circles and stars represent the projectile–target injection points. Panels (a) and (e) show that the tendencies of the driving potential trajectories for these collisions are similar. Two pockets appeared at $\eta = 0.2, 0$ to derive the potentials of the target ^{248}Cm -based reactions. One pocket in the driving potentials for the target ^{232}Th -based reactions appears at $\eta = 0.2$. The neutron subshell number $N = 162$ can potentially play a crucial role in pocket formation. For projectiles, such as ^{208}Po , which are distant from the β -stable line, their initial points of interaction lie significantly away from their respective driving potential trajectories. As diffusion starts, they quickly converge toward the driving potential path. Generally, using the PES, one can broadly predict the spectral distribution trend across each isotope chain.

By solving a set of master equations, we derived the production probabilities of primary fragments with their respective excitation energies. These equations categorized the fragments based on mass number and kinetic energy as delineated in Eq. (16). These distributions are illustrated in Fig. 4, with driving potential trajectories represented as solid gray lines. From Fig. 4, we observe two prominent peaks in the high kinetic regions, situated around the projectile–target injection points. Additionally, cross sections tend to concentrate in the valleys of the driving potential trajectories. Reactions involving projectiles 208

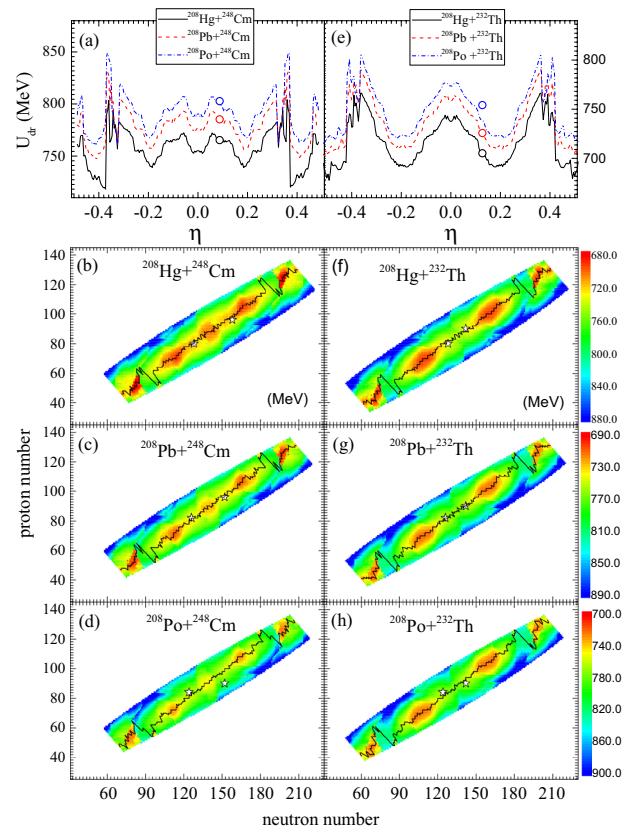


Fig. 3 (Color online) Potential energy surface and driver potentials of projectiles ^{208}Hg -, ^{208}Pb -, and ^{208}Po -induced reactions with targets ^{248}Cm and ^{232}Th at tip–tip collisions are listed in Fig. 3. Specifically, ^{208}Hg -, ^{208}Pb -, and ^{208}Po -induced reactions were represented by solid black, dashed red, and dash-dot blue lines in panels a, e, respectively. Potential energy surfaces for these collisions are shown in panels b–d, f–h, respectively. Open stars denote projectile–target injection points. These solid black lines represent valley trajectories on the two-dimensional potential energy surface

Hg , ^{208}Pb , and ^{208}Po with targets ^{248}Cm and ^{232}Th at the incident energy $E_{c.m.} = 1.1 \times V_B$ exhibited TKE-mass distributions that were both symmetric and expansive. The TKE-mass distribution spans broadly within the kinetic range of 500–800 MeV and mass range of 160–280 MeV, suggesting a potential transfer of more than 30 nucleons.

Utilizing the statistical evaporation program, we calculated the survival probability of the excited primary fragments, which in turn determined the production cross sections of the secondary fragments. The production cross sections of primary and secondary fragments, delineated by mass and charge numbers in the collisions from projectiles ^{208}Hg , ^{208}Pb , and ^{208}Po with target ^{248}Cm at $E_{c.m.} = 1.1 \times V_B$, are depicted in Fig. 5 panels (a) through (f). The solid blue and dashed red lines represent secondary and primary fragments, respectively, while regions of superheavy nuclei are highlighted with rectangular

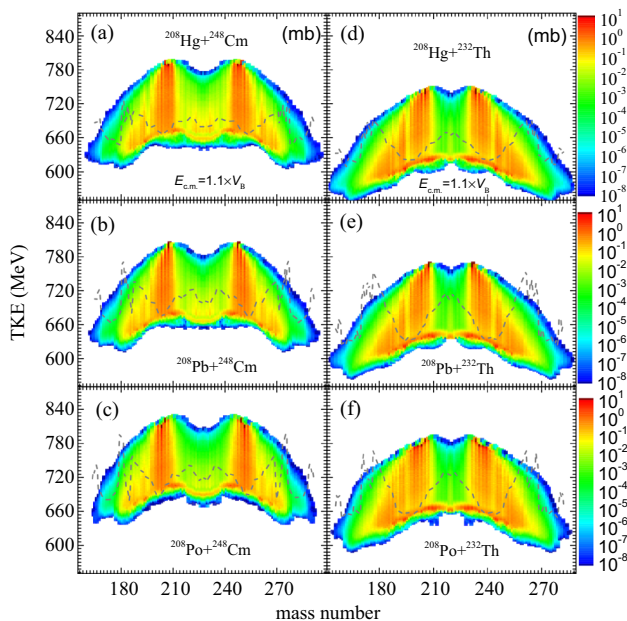


Fig. 4 (Color online) Panels a–f display the calculated TKE-mass distribution of primary reaction products from head-on collisions involving projectiles ^{208}Hg , ^{208}Pb , and ^{208}Po with targets ^{248}Cm and ^{232}Th at $E_{c.m.} = 1.1 \times V_B$. Driving potential trajectories are also incorporated

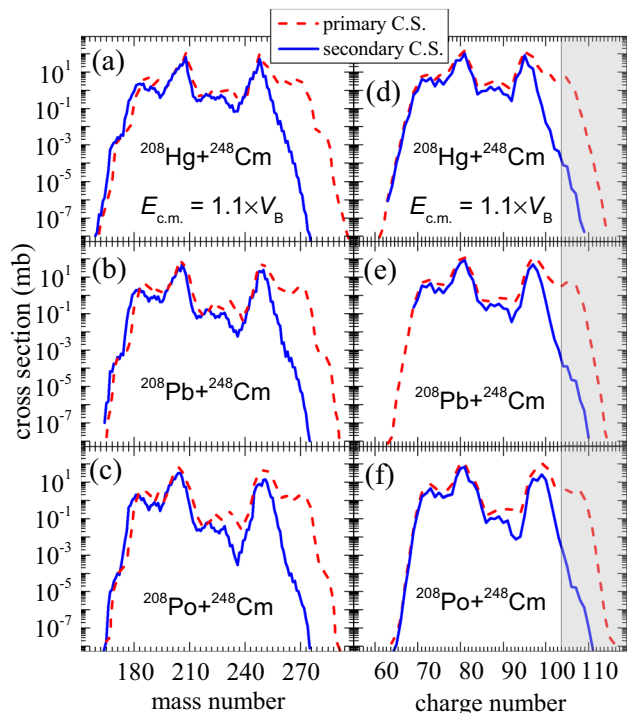


Fig. 5 (Color online) The calculated primary and secondary yields mass and charge distribution for ^{208}Hg -, ^{208}Pb -, and ^{208}Po -induced reactions with targets ^{248}Cm at $E_{c.m.} = 1.1 \times V_B$ were listed in panels a–f, respectively. Dashed red and solid blue lines represented primary and secondary yields. The superheavy region ($Z > 104$) is shown by a rectangular shadow

shading. Our findings show that primary fragments span a vast charge spectrum, even reaching the superheavy regions. Conversely, secondary fragment production was significantly dampened by de-excitation. This reduction is attributed to the fact that highly excited primary trans-target fragments, having minimal fission barriers, are prone to undergoing fission. Our predictions indicate cross sections for superheavy nuclei (with atomic numbers $Z = 104\text{--}116$) exceeding 10 picobarns. The neutron subshell $N = 162$ may be particularly influential, especially in the $^{208}\text{Po} + ^{248}\text{Cm}$ collision.

Secondary production cross sections for actinide target-like fragments, including isotopes of Actinium, Thorium, Protactinium, Uranium, Neptunium, Plutonium, Americium, Curium, Berkelium, Californium, Einsteinium, Fermium, Mendelevium, Nobelium, and Lawrencium, have been calculated. These calculations pertain to collisions involving projectiles ^{208}Pt , ^{208}Hg , ^{208}Pb , ^{208}Po , ^{208}Rn , and ^{208}Ra bombarding on targets ^{248}Cm at $E_{c.m.} = 1.1 \times V_B$. The line representations for these projectiles in Fig. 6 are

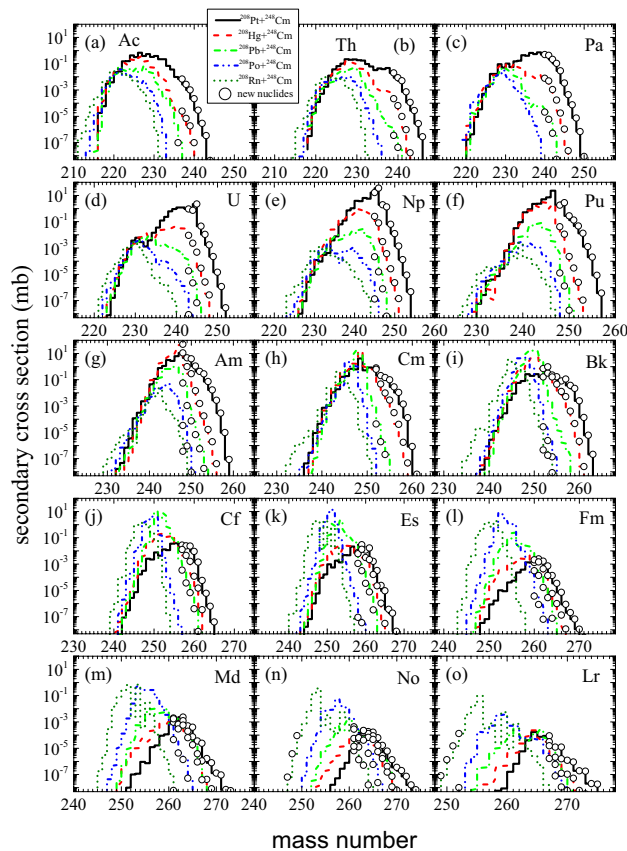


Fig. 6 (Color online) Predicted isotopic distribution cross sections for target-like fragments with atomic numbers $Z = 89\text{--}103$ resulting from the collisions of projectiles Pt, Hg, Pb, Po, and Rn with mass number $A = 208$ bombarding on target ^{248}Cm at $E_{c.m.} = 1.1 \times V_B$. The patterns correspond to the following projectiles: solid black for Pt, dashed red for Hg, dash-dot green for Pb, dashed-dot-dot blue for Po, and short dashed olive for Rn. Predicted new actinide isotopes are highlighted with open circles

as follows: solid black for ^{208}Pt , dashed red for ^{208}Hg , dash-dot green for ^{208}Pb , dashed-dot-dot blue for ^{208}Po , and short dashed olive for ^{208}Rn . Observations indicate that collisions characterized by a smaller Coulomb force lean toward the neutron-rich region, whereas those with a more substantial Coulomb force gravitate to neutron-deficient areas. Numerous previously unidentified actinide isotopes are predicted from reactions $^{208}\text{Pt} + ^{248}\text{Cm}$, $^{208}\text{Hg} + ^{248}\text{Cm}$, $^{208}\text{Pb} + ^{248}\text{Cm}$, $^{208}\text{Po} + ^{248}\text{Cm}$, $^{208}\text{Rn} + ^{248}\text{Cm}$, and $^{208}\text{Ra} + ^{248}\text{Cm}$. These predictions are detailed in Table 1. For the new neutron-rich actinide isotopes, $^{208}\text{Pt} + ^{248}\text{Cm}$ reactions produce the largest cross sections. However, ^{208}Pt remains unclear. Notably, unknown actinide products are highly dependent on the Coulomb potential. The $^{208}\text{Rn} + ^{248}\text{Cm}$ reactions result in the largest cross sections for new neutron-deficient actinide

isotopes. The open circles represent the new neutron-rich actinide nuclides.

Figure 7 shows secondary production cross sections of all the formed fragments in collisions of $^{208}\text{Os} + ^{248}\text{Cm}$, $^{208}\text{Pt} + ^{248}\text{Cm}$, $^{208}\text{Hg} + ^{248}\text{Cm}$, $^{208}\text{Pb} + ^{248}\text{Cm}$, $^{208}\text{Po} + ^{248}\text{Cm}$, $^{208}\text{Rn} + ^{248}\text{Cm}$, $^{208}\text{Ra} + ^{248}\text{Cm}$, and primary production cross sections of $^{208}\text{Pb} + ^{248}\text{Cm}$ at the incident energy $E_{\text{c.m.}} = 1.1 \times V_{\text{B}}$ as N - Z panel. Panels (g) and (h) clearly show the de-excitation effects. Panels (a), (b), (c), (d), (e), (f), and (h) show that many new isotopes are predicted, including neutron-rich and neutron-deficient isotopes and even superheavy nuclei. The projectile–target injection points and all existing isotopes in the nuclide chart are represented by solid black triangles and open squares, respectively.

Fig. 7 (Color online) The production cross sections of all secondary fragments formed in the collisions involving $^{208}\text{Pt} + ^{248}\text{Cm}$, $^{208}\text{Hg} + ^{248}\text{Cm}$, $^{208}\text{Pb} + ^{248}\text{Cm}$, $^{208}\text{Po} + ^{248}\text{Cm}$, $^{208}\text{Rn} + ^{248}\text{Cm}$, and $^{208}\text{Ra} + ^{248}\text{Cm}$ at the incident energy $E_{\text{c.m.}} = 1.1 \times V_{\text{B}}$ along with the primary fragments from $^{208}\text{Pb} + ^{248}\text{Cm}$ are listed in N - Z panels. Open stars denote projectile–target injection points

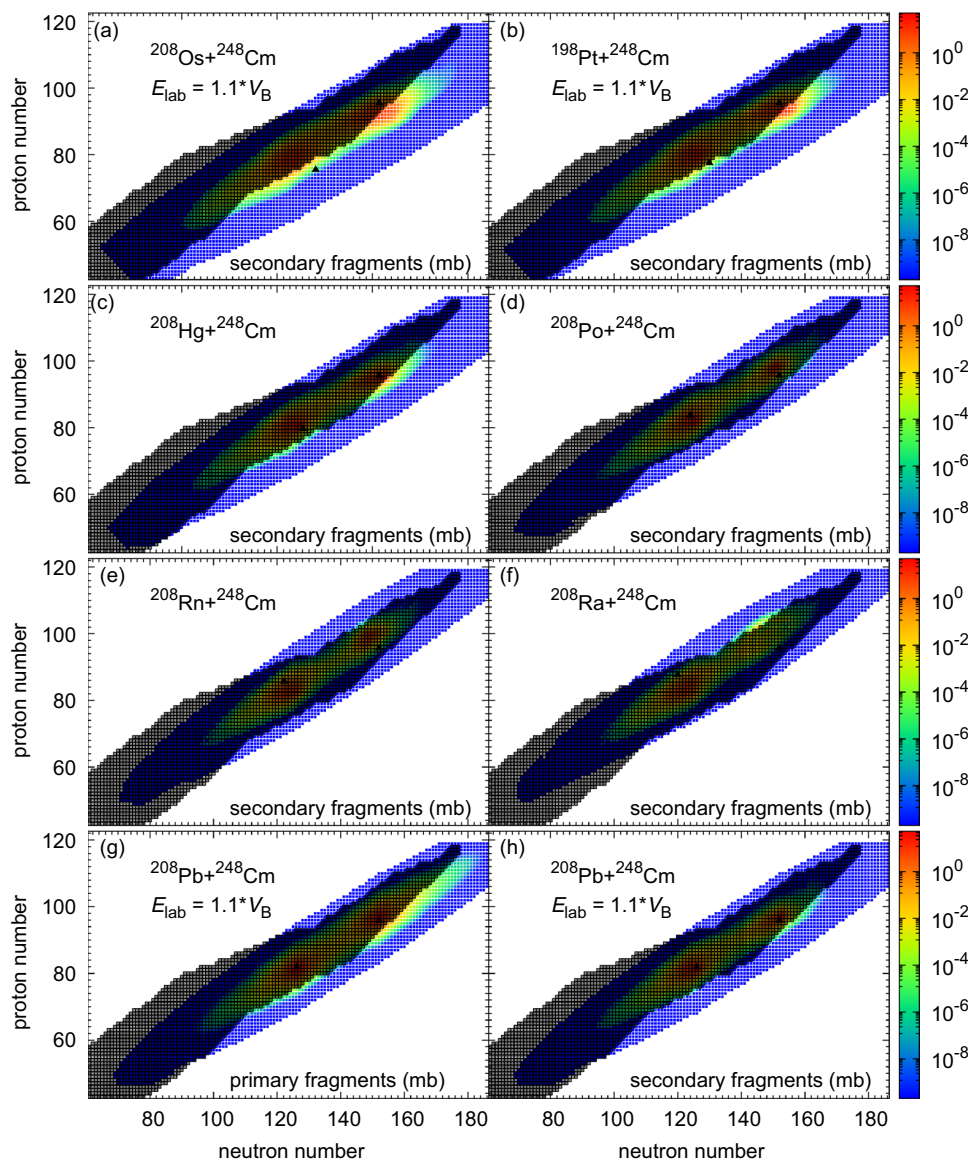


Table 1 Calculated cross sections of unknown actinide isotopes with $Z = 89\text{--}103$ in the reactions of projectiles ^{208}Pt -, ^{208}Hg -, and ^{208}Pb -induced MNT reactions with target ^{248}Cm at incident energy $E_{\text{c.m.}} = 1.1 \times V_{\text{B}}$

$^{248}\text{Cm} +$	^{208}Pt	^{208}Hg	^{208}Pb	$^{248}\text{Cm} +$	^{208}Pt	^{208}Hg	^{208}Pb	$^{248}\text{Cm} +$	^{208}Pt	^{208}Hg	^{208}Pb
^{237}Ac	6.8 μb	24 nb		^{254}Pu	1.3 μb			^{261}Es	16 μb	2.2 μb	7.6 nb
^{238}Ac	2.6 μb	6.9 nb		^{255}Pu	0.2 μb			^{262}Es	0.2 μb	0.1 μb	0.3 nb
^{239}Ac	1 μb	1.8 nb		^{256}Pu	8.4 nb			^{263}Es	0.3 μb	22 nb	0.1 nb
^{240}Ac	28 nb	0.1 nb		^{248}Am	11 mb	50 mb	56 μb	^{264}Es	23 nb	1.1 nb	30 pb
^{241}Ac	2.8 nb	0.5 pb		^{249}Am	4.5 mb	1 mb	1.1 μb	^{265}Es	9.2 nb	30 pb	
^{239}Th	20 μb	0.2 μb	0.34 nb	^{250}Am	3.9 mb	0.3 mb	74 nb	^{260}Fm	1.3 μb	2.1 μb	0.3 μb
^{240}Th	8.4 μb	64.8 nb	0.04 nb	^{251}Am	1.1 mb	14 μb	6.6 nb	^{261}Fm	2.4 μb	1.4 μb	0.1 μb
^{241}Th	5 μb	9.6 nb		^{252}Am	0.4 mb	1.5 μb		^{262}Fm	1.6 μb	0.4 μb	16 nb
^{242}Th	0.7 μb	0.94 nb		^{253}Am	0.3 mb	0.2 μb		^{263}Fm	0.7 μb	0.1 μb	2.8 nb
^{243}Th	0.1 μb	0.02 nb		^{254}Am	72 μb	16 nb		^{264}Fm	0.1 μb	5.8 nb	0.08 nb
^{244}Th	26 nb			^{255}Am	17 μb	1.9 nb		^{265}Fm	34 nb	0.9 nb	
^{245}Th	2.8 nb			^{256}Am	2.7 μb	40 pb		^{266}Fm	7 nb	0.1 nb	
^{246}Th	0.3 nb			^{257}Am	0.3 μb			^{267}Fm	0.9 nb	10 pb	
^{240}Pa	0.5 mb	7.8 μb	20. nb	^{258}Am	9.7 nb			^{261}Md	0.9 μb	1.9 μb	1.7 μb
^{241}Pa	0.4 mb	4.9 μb	5.5 nb	^{252}Cm	0.8 mb	0.6 mb	43 nb	^{262}Md	0.6 μb	0.6 μb	0.2 μb
^{242}Pa	0.2 mb	1.1 μb	0.5 nb	^{253}Cm	0.2 mb	47 μb	1.9 nb	^{263}Md	2.3 μb	1.2 μb	0.5 μb
^{243}Pa	10 μb	0.2 μb	5 pb	^{254}Cm	0.1 mb	9.7 μb	0.2 nb	^{264}Md	0.5 μb	0.2 μb	62 nb
^{244}Pa	28 μb	17 nb		^{255}Cm	97 μb	2.8 μb	2 pb	^{265}Md	0.4 μb	74 nb	18 nb
^{245}Pa	3.3 μb	1 nb		^{256}Cm	28 μb	0.3 μb		^{266}Md	35 nb	3.7 nb	0.9 nb
^{246}Pa	0.4 μb	20 pb		^{257}Cm	11 μb	40 nb		^{267}Md	23 nb	1.1 nb	40 pb
^{247}Pa	74 nb			^{258}Cm	1.4 μb	1.7 nb		^{268}Md	1.6 nb	40 pb	
^{248}Pa	7.3 nb			^{259}Cm	0.1 μb	40 pb		^{269}Md	0.7 nb	8 pb	
^{249}Pa	0.6 nb			^{260}Cm	0.8 nb			^{261}No	6.3 nb	54 nb	47 nb
^{250}Pa	9 pb			^{252}Bk	0.2 mb	0.7 mb	36 μb	^{262}No	12 nb	64 nb	219 nb
^{243}U	0.9 mb	9.1 μb	18.4 nb	^{253}Bk	0.3 mb	0.9 mb	1.9 μb	^{263}No	0.1 nb	206 nb	68 nb
^{244}U	0.7 mb	2.2 μb	2.2 nb	^{254}Bk	0.2 mb	0.1 mb	0.1 μb	^{264}No	0.2 nb	131 nb	47 nb
^{245}U	2.2 mb	0.5 μb	70 pb	^{255}Bk	0.1 mb	46 μb	14 nb	^{265}No	0.1 nb	86 nb	5.4 nb
^{246}U	46 μb	29 nb		^{256}Bk	81 μb	12 μb	1.5 nb	^{266}No	62 nb	16 nb	0.15 nb
^{247}U	10 μb	2.6 nb		^{257}Bk	0.1 mb	5.2 μb	0.3 nb	^{267}No	16 nb	2.6 nb	0.01 nb
^{248}U	1.7 μb	0.3 nb		^{258}Bk	36 μb	0.4 μb	3 pb	^{268}No	6 nb	0.4 nb	
^{249}U	0.2 μb			^{259}Bk	22 μb	46 nb		^{269}No	1.3 nb	70 pb	
^{250}U	14 nb			^{260}Bk	2.5 μb	2. nb		^{267}Lr	86 nb	31 nb	15 nb
^{251}U	1.1 nb			^{261}Bk	0.1 μb	20 pb		^{268}Lr	12 nb	2.1 nb	0.6 nb
^{245}Np	3.3 μb	1 nb		^{261}Bk	6.1 nb			^{269}Lr	17 nb	1.5 nb	0.1 nb
^{246}Np	4.3 μb	20 pb		^{257}Cf	27 μb	12 μb	0.3 μb	^{270}Lr	1.2 nb	0.1 nb	6 pb
^{247}Np	74 nb			^{258}Cf	24 μb	4.5 μb	36 nb	^{271}Lr	0.9 nb	80 pb	1 pb
^{248}Np	7.3 nb			^{259}Cf	23 μb	1.6 μb	6.5 nb				
^{249}Np	0.7 nb			^{260}Cf	9.2 μb	0.1 μb	0.4 nb				
^{248}Pu	17 mb	41 μb	12.8 nb	^{261}Cf	1.4 μb	15 nb	7 pb				
^{249}Pu	2.7 mb	11 μb	1.3 nb	^{262}Cf	6.1 nb	0.3 nb					
^{250}Pu	0.3 mb	0.2 μb	0.019 nb	^{263}Cf	0.6 nb						
^{251}Pu	0.1 mb	30 nb		^{258}Es	7.4 μb	6.2 μb	1.1 μb				
^{252}Pu	48 μb	2.4 nb		^{259}Es	29 μb	13 μb	0.3 μb				
^{253}Pu	13 μb	10 pb		^{260}Es	11 μb	3 μb	34 nb				

4 Conclusion

Using the DNS model framework, we systematically calculated the production cross sections of MNT fragments in reactions involving projectiles such as ^{208}Os , ^{208}Pt , ^{208}Hg , ^{208}Pb , ^{208}Po , ^{208}Rn , ^{208}Ra , and $^{132,136}\text{Xe}$ colliding with targets ^{232}Th and ^{248}Cm around Coulomb barrier energies. To investigate the isospin diffusion on the formation of actinide products during the MNT process, the same number of projectiles with $A = 208$ was selected. Our calculation for $^{132,136}\text{Xe} + ^{248}\text{Cm}$ is consistent with the available experimental data. The sticking time for these colliding systems, inferred from deflection functions, was significantly influenced by the Coulomb force, especially at smaller impact parameters. Furthermore, PES and TKE of these reactions, which can contribute to predicting the tendency of cross-sectional diffusion, are discussed. A relatively large cross section from TKE appears around the pockets in PES, where the neutron subshell $N = 162$ is evident. The de-excitation process strongly depresses the primary cross section of actinide isotopes up to four magnitude levels. The production cross section of the new actinides is highly dependent on the N/Z ratio of the isobaric projectile. It was determined that the Coulomb force coupled with the shell effect plays a crucial role in the production of cross sections of actinides products in MNT reactions. These five colliding systems predicted a wide array of previously unknown heavy isotopes, with accessible cross-sectional values even for superheavy nuclei within the charge numbers $Z = 104\text{--}110$.

Author contributions All authors contributed to the study conception and design. Material preparation, data collection, and analysis were performed by Chang Geng and Peng-Hui Chen. The first draft of the manuscript was written by Peng-Hui Chen and Chang Geng, and all authors commented on previous versions of the manuscript. All authors read and approved the final manuscript.

Data availability The data that support the findings of this study are openly available in Science Data Bank at <https://doi.org/10.57760/sciencedb.j00186.00249> and <https://cstr.cn/31253.11.sciencedb.j00186.00249>.

Declarations

Conflict of interest The authors declare that they have no competing interests.

References

1. K. Auranen, A.D. Briscoe, L.S. Ferreira et al., Nanosecond-scale proton emission from strongly oblate-deformed ^{149}Lu . *Phys. Rev. Lett.* **128**, 112501 (2022). <https://doi.org/10.1103/PhysRevLett.128.112501>
2. H.B. Yang, Z.G. Gan, Z.Y. Zhang et al., New isotope ^{207}Th and odd-even staggering in α -decay energies for nuclei with $Z > 82$ and $N < 126$. *Phys. Rev. C* **105**, L051302 (2022). <https://doi.org/10.1103/PhysRevC.105.L051302>
3. T. Huang, D. Seweryniak, B.B. Back et al., Discovery of the new isotope ^{251}Lr : impact of the hexacontetrapole deformation on single-proton orbital energies near the $z = 100$ deformed shell gap. *Phys. Rev. C* **106**, L061301 (2022). <https://doi.org/10.1103/PhysRevC.106.L061301>
4. Y.T. Oganessian, V.K. Utyonkov, N.D. Kovrizhnykh et al., First experiment at the super heavy element factory: high cross section of ^{288}Mc in the $^{243}\text{Am} + ^{48}\text{Ca}$ reaction and identification of the new isotope ^{264}Lr . *Phys. Rev. C* **106**, L031301 (2022). <https://doi.org/10.1103/PhysRevC.106.L031301>
5. G.G. Kiss, A. Vitez-Sveicz, Y. Saito et al., Measuring the beta-decay properties of neutron-rich exotic Pm, Sm, Eu, and Gd isotopes to constrain the nucleosynthesis yields in the rare-earth region. *Astrophys. J.* **936**, 107 (2022). <https://doi.org/10.3847/1538-4357/ac80fc>
6. M. Huang, Z. Gan, Z. Zhang et al., Alpha decay of the new isotope ^{204}Ac . *Phys. Lett. B* **834**, 137484 (2022). <https://doi.org/10.1016/j.physletb.2022.137484>
7. D.S. Ahn, J. Amano, H. Baba et al., Discovery of ^{39}Na . *Phys. Rev. Lett.* **129**, 212502 (2022). <https://doi.org/10.1103/PhysRevLett.129.212502>
8. Y.T. Oganessian, V.K. Utyonkov, N.D. Kovrizhnykh et al., New isotope ^{286}Mc produced in the $^{243}\text{Am} + ^{48}\text{Ca}$ reaction. *Phys. Rev. C* **106**, 064306 (2022). <https://doi.org/10.1103/PhysRevC.106.064306>
9. M. Thoennessen, *The Discovery of Isotopes* (Springer, Berlin, 2016)
10. K.Y. Zhang, M.K. Cheoun, Y.B. Choi et al., Nuclear mass table in deformed relativistic Hartree–Bogoliubov theory in continuum, I: even–even nuclei. *At. Data Nucl. Data* **144**, 101488 (2022). <https://doi.org/10.1016/j.adt.2022.101488>
11. P. Möller, A.J. Sierk, T. Ichikawa et al., Nuclear ground-state masses and deformations: FRDM(2012). *At. Data Nucl. Data* **109–110**, 1–204 (2016). <https://doi.org/10.1016/j.adt.2015.10.002>
12. P. Jachimowicz, M. Kowal, J. Skalski, Properties of heaviest nuclei with $98 \leq Z \leq 126$ and $134 \leq N \leq 192$. *At. Data Nucl. Data* **138**, 101393 (2021). <https://doi.org/10.1016/j.adt.2020.101393>
13. A. Sămark-Roth, D.M. Cox, D. Rudolph et al., Spectroscopy along flerovium decay chains: Discovery of ^{280}Ds and an excited state in ^{282}Cn . *Phys. Rev. Lett.* **126**, 032503 (2021). <https://doi.org/10.1103/PhysRevLett.126.032503>
14. Z.Y. Zhang, H.B. Yang, M.H. Huang et al., New α -emitting isotope ^{214}U and abnormal enhancement of α -particle clustering in lightest uranium isotopes. *Phys. Rev. Lett.* **126**, 152502 (2021). <https://doi.org/10.1103/PhysRevLett.126.152502>
15. J. Khuyagbaatar, F.P. Heßberger, S. Hofmann et al., α decay of $^{243}\text{Fm}_{143}$ and $^{245}\text{Fm}_{145}$, and of their daughter nuclei. *Phys. Rev. C* **102**, 044312 (2020). <https://doi.org/10.1103/PhysRevC.102.044312>
16. N. Fukuda, T. Kubo, D. Kameda et al., Identification of new neutron-rich isotopes in the rare-earth region produced by 345 MeV/nucleon ^{238}U . *J. Phys. Soc. J.* **87**, 014202 (2018). <https://doi.org/10.7566/JPSJ.87.014202>
17. H.M. Devaraja, S. Heinz, O. Beliuskina et al., Observation of new neutron-deficient isotopes with $Z \geq 92$ in multinucleon transfer reactions. *Phys. Lett. B* **748**, 199–203 (2015). <https://doi.org/10.1016/j.physletb.2015.07.006>
18. F.P. Hessberger, V. Ninov, D. Ackermann et al., Production of heavy residues in nuclear collisions leading to $Z_p + Z_t \geq 75$ at bombarding energies of $E/A = (11.4\text{--}15.3)\text{MeV/u}$. *Nucl. Phys.*

- A **568**, 121–140 (1994). [https://doi.org/10.1016/0375-9474\(94\)90007-8](https://doi.org/10.1016/0375-9474(94)90007-8)
19. A. Winther, Dissipation, polarization and fluctuation in grazing heavy-ion collisions and the boundary to the chaotic regime. *Nucl. Phys. A* **594**, 203–245 (1995). [https://doi.org/10.1016/0375-9474\(95\)00374-A](https://doi.org/10.1016/0375-9474(95)00374-A)
 20. A. Winther, Grazing reactions in collisions between heavy nuclei. *Nucl. Phys. A* **572**, 191–235 (1994). [https://doi.org/10.1016/0375-9474\(94\)90430-8](https://doi.org/10.1016/0375-9474(94)90430-8)
 21. Z.Q. Feng, G.M. Jin, J.Q. Li, Production of heavy isotopes in transfer reactions by collisions of $^{238}\text{U}+^{238}\text{U}$. *Phys. Rev. C* **80**, 067601 (2009). <https://doi.org/10.1103/PhysRevC.80.067601>
 22. Z.Q. Feng, Production of neutron-rich isotopes around $N = 126$ in multinucleon transfer reactions. *Phys. Rev. C* **95**, 024615 (2017). <https://doi.org/10.1103/PhysRevC.95.024615>
 23. M. Huang, Z. Gan, X. Zhou et al., Competing fusion and quasifission reaction mechanisms in the production of superheavy nuclei. *Phys. Rev. C* **82**, 044614 (2010). <https://doi.org/10.1103/PhysRevC.82.044614>
 24. L. Zhu, P.W. Wen, C.J. Lin et al., Shell effects in a multinucleon transfer process. *Phys. Rev. C* **97**, 044614 (2018). <https://doi.org/10.1103/PhysRevC.97.044614>
 25. X.Q. Deng, S.G. Zhou, Examination of promising reactions with ^{241}Am and ^{244}Cm targets for the synthesis of new superheavy elements within the dinuclear system model with a dynamical potential energy surface. *Phys. Rev. C* **107**, 014616 (2023). <https://doi.org/10.1103/PhysRevC.107.014616>
 26. X.B. Yu, L. Zhu, Z.H. Wu et al., Predictions for production of superheavy nuclei with $Z = 105$ – 112 in hot fusion reactions. *Nucl. Sci. Tech.* **29**, 154 (2018). <https://doi.org/10.1007/s41365-018-0501-2>
 27. P.H. Chen, F. Niu, Y.F. Guo et al., Nuclear dynamics in multinucleon transfer reactions near coulomb barrier energies. *Nucl. Sci. Tech.* **29**, 185 (2018). <https://doi.org/10.1007/s41365-018-0521-y>
 28. F. Niu, P.H. Chen, H.G. Cheng et al., Multinucleon transfer dynamics in nearly symmetric nuclear reactions. *Nucl. Sci. Tech.* **31**, 59 (2020). <https://doi.org/10.1007/s41365-020-00770-1>
 29. F. Niu, P.H. Chen, Z.Q. Feng, Systematics on production of superheavy nuclei $Z = 119$ – 122 in fusion-evaporation reactions. *Nucl. Sci. Tech.* **32**, 103 (2021). <https://doi.org/10.1007/s41365-021-00946-3>
 30. P.H. Chen, H. Wu, Z.X. Yang et al., Prediction of synthesis cross sections of new moscovium isotopes in fusion-evaporation reactions. *Nucl. Sci. Tech.* **34**, 7 (2023). <https://doi.org/10.1007/s41365-022-01157-0>
 31. V. Zagrebaev, W. Greiner, Cross sections for the production of superheavy nuclei. *Nucl. Phys. A* **944**, 257–307 (2015). <https://doi.org/10.1016/j.nuclphysa.2015.02.010>. (**Special Issue on Superheavy Elements**)
 32. D. Boilley, B. Cauchois, H. Lü et al., How accurately can we predict synthesis cross sections of superheavy elements? *Nucl. Sci. Tech.* (2018). <https://doi.org/10.1007/s41365-018-0509-7>
 33. C. Golabek, C. Simenel, Collision dynamics of two ^{238}U atomic nuclei. *Phys. Rev. Lett.* **103**, 042701 (2009). <https://doi.org/10.1103/PhysRevLett.103.042701>
 34. C. Simenel, Particle-number fluctuations and correlations in transfer reactions obtained using the Balian-Vénéroni variational principle. *Phys. Rev. Lett.* **106**, 112502 (2011). <https://doi.org/10.1103/PhysRevLett.106.112502>
 35. X. Jiang, N. Wang, Production mechanism of neutron-rich nuclei around $N = 126$ in the multi-nucleon transfer reaction $^{132}\text{Sn} + ^{208}\text{Pb}$. *Chin. Phys. C* **42**, 104105 (2018). <https://doi.org/10.1088/1674-1137/42/10/104105>
 36. J.L. Tian, X.Z. Wu, K. Zhao et al., Properties of the composite systems formed in the reactions of $^{238}\text{U}+^{238}\text{U}$ and $^{232}\text{Th}+^{250}\text{Cf}$. *Phys. Rev. C* **77**, 064603 (2008). <https://doi.org/10.1103/PhysRevC.77.064603>
 37. K. Zhao, Z.X. Li, X.Z. Wu et al., Production probability of superheavy fragments at various initial deformations and orientations in the $^{238}\text{U}+^{238}\text{U}$ reaction. *Phys. Rev. C* **88**, 044605 (2013). <https://doi.org/10.1103/PhysRevC.88.044605>
 38. V.V. Volkov, Deep inelastic transfer reactions—the new type of reactions between complex nuclei. *Phys. Rep.* **44**, 93–157 (1978). [https://doi.org/10.1016/0370-1573\(78\)90200-4](https://doi.org/10.1016/0370-1573(78)90200-4)
 39. G.G. Adamian, N.V. Antonenko, W. Scheid et al., Treatment of competition between complete fusion and quasifission in collisions of heavy nuclei. *Nucl. Phys. A* **627**, 361–378 (1997). [https://doi.org/10.1016/S0375-9474\(97\)00605-2](https://doi.org/10.1016/S0375-9474(97)00605-2)
 40. G.G. Adamian, N.V. Antonenko, W. Scheid et al., Fusion cross sections for superheavy nuclei in the dinuclear system concept. *Nucl. Phys. A* **633**, 409–420 (1998). [https://doi.org/10.1016/S0375-9474\(98\)00124-9](https://doi.org/10.1016/S0375-9474(98)00124-9)
 41. Z.Q. Feng, G.M. Jin, J.Q. Li et al., Formation of superheavy nuclei in cold fusion reactions. *Phys. Rev. C* **76**, 044606 (2007). <https://doi.org/10.1103/PhysRevC.76.044606>
 42. Z.Q. Feng, G.M. Jin, F. Fu et al., Production cross sections of superheavy nuclei based on dinuclear system model. *Nucl. Phys. A* **771**, 50–67 (2006). <https://doi.org/10.1016/j.nuclphysa.2006.03.002>
 43. P.H. Chen, F. Niu, W. Zuo et al., Approaching the neutron-rich heavy and superheavy nuclei by multinucleon transfer reactions with radioactive isotopes. *Phys. Rev. C* **101**, 024610 (2020). <https://doi.org/10.1103/PhysRevC.101.024610>
 44. P.H. Chen, Z.Q. Feng, J.Q. Li et al., A statistical approach to describe highly excited heavy and superheavy nuclei. *Chin. Phys. C* **40**, 091002 (2016). <https://doi.org/10.1088/1674-1137/40/9/091002>
 45. G.G. Adamian, N.V. Antonenko, W. Scheid, Characteristics of quasifission products within the dinuclear system model. *Phys. Rev. C* **68**, 034601 (2003). <https://doi.org/10.1103/PhysRevC.68.034601>
 46. P. Grangé, L. Jun-Qing, H.A. Weidenmüller, Induced nuclear fission viewed as a diffusion process: transients. *Phys. Rev. C* **27**, 2063–2077 (1983). <https://doi.org/10.1103/PhysRevC.27.2063>
 47. P.H. Chen, Z.Q. Feng, F. Niu et al., Production of proton-rich nuclei around $Z = 84$ – 90 in fusion-evaporation reactions. *Eur. Phys. J. A* (2017). <https://doi.org/10.1140/epja/i2017-12281-x>
 48. W. Nörenberg, Quantum-statistical approach to gross properties of peripheral collisions between heavy nuclei. *Z. Phys. A* **274**, 241–250 (1975). <https://doi.org/10.1007/BF01437736>
 49. J.Q. Li, G. Wolschin, Distribution of the dissipated angular momentum in heavy-ion collisions. *Phys. Rev. C* **27**, 590–601 (1983). <https://doi.org/10.1103/PhysRevC.27.590>
 50. W.F. Li, N. Wang, J.F. Li et al., Fusion probability in heavy-ion collisions by a dinuclear-system model. *Eur. Phys. Lett. (EPL)* **64**, 750–756 (2003). <https://doi.org/10.1209/epl/i2003-00622-0>
 51. G. Wolschin, W. Nörenberg, Analysis of relaxation phenomena in heavy-ion collisions. *Z. Phys. A* **284**, 209–216 (1978). <https://doi.org/10.1140/epja/i2017-12281-x>
 52. C.Y. Wong, Interaction barrier in charged-particle nuclear reactions. *Phys. Rev. Lett.* **31**, 766–769 (1973). <https://doi.org/10.1103/PhysRevLett.31.766>
 53. I.I. Gontchar, D.J. Hinde, M. Dasgupta et al., Double folding nucleus–nucleus potential applied to heavy-ion fusion reactions. *Phys. Rev. C* **69**, 024610 (2004). <https://doi.org/10.1103/PhysRevC.69.024610>
 54. P. Möller, Nuclear ground-state masses and deformations. *At. Data Nucl. Data Tables* **59**, 185–381 (1995). <https://doi.org/10.1006/adnd.1995.1002>

55. P. Demetriou, S. Goriely, Microscopic nuclear level densities for practical applications. *Nucl. Phys. A* **695**, 95–108 (2001). [https://doi.org/10.1016/S0375-9474\(01\)01095-8](https://doi.org/10.1016/S0375-9474(01)01095-8)
56. S. Cohen, W.J. Swiatecki, The deformation energy of a charged drop: part V: results of electronic computer studies. *Ann. Phys.* **22**, 406–437 (1963). [https://doi.org/10.1016/0003-4916\(63\)90385-3](https://doi.org/10.1016/0003-4916(63)90385-3)
57. G.G. Adamian, N.V. Antonenko, S.P. Ivanova et al., Analysis of survival probability of superheavy nuclei. *Phys. Rev. C* **62**, 064303 (2000). <https://doi.org/10.1103/PhysRevC.62.064303>
58. J.D. Jackson, A schematic model for (p, xn) cross sections in heavy elements. *Can. J. Phys.* **34**, 767–779 (1956). <https://doi.org/10.1139/p56-087>
59. R.B. Welch, K.J. Moody, K.E. Gregorich et al., Dependence of actinide production on the mass number of the projectile: $\text{Xe} + ^{248}\text{Cm}$. *Phys. Rev. C* **35**, 204–212 (1987). <https://doi.org/10.1103/PhysRevC.35.204>
60. K.J. Moody, D. Lee, R.B. Welch et al., Actinide production in reactions of heavy ions with ^{248}Cm . *Phys. Rev. C* **33**, 1315–1324 (1986). <https://doi.org/10.1103/PhysRevC.33.1315>

Springer Nature or its licensor (e.g. a society or other partner) holds exclusive rights to this article under a publishing agreement with the author(s) or other rightsholder(s); author self-archiving of the accepted manuscript version of this article is solely governed by the terms of such publishing agreement and applicable law.